Supplementary Information for

Differences and potential driving mechanisms of marine bloom patterns between hemispheres

Wei Hu *et al.*

**Jian-rong Ma, Bo-qiang Qin.
Email: majianrong@cigit.ac.cn, qinbq@niglas.ac.cn

This PDF file includes:

Supplementary Text
Figs. S1 to S20
Tables S1 to S13
References (1 to 15)

Supplementary Text

The changing trend of environmental factors

With respect to the worldwide distribution of ocean surface temperatures (Figures S11a and S11b), the average daily temperature exceeds 24 ℃ in many regions, particularly along the coasts of the Middle East, Somalia, northeastern Australia, Madagascar, and the central Atlantic and Pacific. This temperature range supports the development and reproduction of algae. The only regions with average nighttime temperatures above 24 ℃ are the Red Sea, Persian Gulf, and Gulf of Oman. All other regions have nighttime temperatures below this threshold. At latitudes above 50° north and south, both daily highs and overnight lows are essentially below freezing. The trend in ocean surface temperature clearly indicates global warming (Figures S11c and S11d). Over half of the oceans' surfaces show an increasing trend in mean annual daylight temperature, with notable exceptions being the Mediterranean Sea, the Gulf of Alaska, the central North Atlantic, the African coast of the South Atlantic, and the Arctic and Antarctic regions. The daily average annual temperature exhibits a significant downward trend in most equatorial regions, the northern Atlantic Ocean, most of the Indian Ocean, the coast of Southeast Asia, the coast of eastern China, the southeastern coast of the United States, and the northern coast of Latin America. In contrast to the annual average daytime temperature, the coastal regions of western Africa, southern Australia, and northern Latin America show a trend where a significant increase in daytime temperature shifts to a significant decrease in nighttime temperature, resulting in a larger diurnal temperature range.

The greatest values are found in the vicinity of the westerly belt, regardless of the time of day and night. High-value wind speed centers, with wind speeds above 11 m s^{-1}, simultaneously occur in the northern seas of Latin America, the coast of Peru, the central Pacific Ocean, and the central Indian Ocean. Conversely, low-value centers, with wind speeds less than 4 m s^{-1}, appear in Southeast Asia, the western coast of South America, and the northwest coast of Latin America (Figures S12a and S12b). The regions that exhibited rising and decreasing trends in wind speed variations across the research period are generally near one another, forming a dispersed block distribution pattern (Figures S12c and S12d).

Throughout the research period, there was a notable decrease in daytime wind speed along the western coast of North America, the central Indian Ocean, the Arabian Gulf, most of the western African coastlines, and the northwest and southeast coasts of South America. Conversely, there was a significant increase in daytime wind speed on the east coast of North America, the northeast and southwest coasts of South America, the north and east coasts of Africa, the Bay of Bengal, the southern coast of Southeast Asia, and most of Oceania's coasts. Wind speed variations in the Pacific Ocean exhibit greater erratic behavior, with a downward trend in the northern hemisphere and an upward trend in the southern hemisphere. The nighttime wind speed trend generally aligns with the daytime trend; however, the decrease in nighttime wind speed is more pronounced than during the day. Additionally, there are regions where the daytime and nighttime wind speed trends are reversed. For instance, in the coastal region of southwest Africa, daytime wind speed is trending upward, while nighttime wind speed is trending downward. This pattern is also observed in the coastal regions of Peru and Chile in South America.

The geographical distribution map of precipitation (Figures S13a) shows that the equatorial rain belt is the location of the peak annual precipitation, with a maximum of around 10712 mm yr^{-1}, and that this belt is shifting northward. The east coasts of the temperate zone continents receive higher summer precipitation due to monsoons and warm currents, in addition to the comparatively high yearly rainfall near the equator. Consequently, these regions see annual precipitation exceeding 1,000 mm. In contrast, the west coasts of continents receive significantly less rainfall than the east coasts due to the absence of rainfall-promoting elements. Southeast Asia, regardless of coastal orientation, receives between 1,500 and 2,000 mm of precipitation annually. The Arctic regions and the subtropical regions along the continent's western coast are home to areas with minimal rainfall. During the research period, there was a noticeable upward trend in annual precipitation in the polar areas. However, a distinct 'Matthew effect' was observed, indicating an increasing trend in regions already experiencing high annual rainfall. Conversely, in smaller regions, annual rainfall trends showed polarization and a downward trend (Figure S13b).

The global oceans' pH ranges primarily between 7.90 and 8.15, with the majority falling between 8.05 and 8.10. In the coastal zones of Southeast Asia, the pH ranges from 8.10 to 8.20, while it decreases toward the equator, averaging between 7.90 and 8.05 (Figure S14a). Additionally, high pH values are observed in the Arctic seas, the Mediterranean Sea, the northern coast of East Asia, the southern coast of Africa, the east and west coasts of southern South America, the central North Pacific, and the central North Atlantic. A significant declining trend in pH is evident across most of the world's oceans, indicating a trend toward acidification. Only a very small portion of the marine regions show an increasing trend in pH values. For example, the western Gulf of Alaska and the Bering Sea exhibit a noticeable upward trend in pH values (Figure S14b).

Global ocean salinity predominantly ranges between 34 and 36g kg^{-1} (Figure S15a). The lowest average salinity value is 6.455g kg^{-1}, which occurs near the Baltic Sea, while the highest average salinity value is 40.82g kg^{-1}, which occurs near the Mediterranean Sea. The Red Sea and Persian Gulf also have higher salinity. In addition, within the range of 40°N-30°S in the Atlantic Ocean, the water salinity is basically 36-38g kg^{-1}. High salinity values are also present in parts of the Arabian Sea, the South Pacific, and the central regions of the South Indian Ocean. During the study period, only a small number of water bodies exhibited significant trends in salinity increase or decrease, with a relatively dispersed distribution. For instance, the North Atlantic waters near Europe showed a significant or highly significant decreasing trend, whereas the waters near the United States and Mexico exhibited a significant or highly significant increasing trend. Most of the global ocean salinity did not show significant changes over the study period. Notably, salinity in the Yellow Sea and the western Indian Ocean demonstrated significant or highly significant decreasing trends, while salinity in some waters west of South America and the coastal zones of southern

Africa showed increasing trends (Figure S15b).

The distribution of solar radiation primarily follows latitudinal zones; however, in the tropics, solar radiation is higher in open waters, exceeding 24×10^6 J m^{-2}, and lower in waters close to the continental coast, primarily within the range of 22×10^6 J m^{-2} ~ 24×10^6 J m^{-2} (Figure S16a). The trend of solar radiation over the study period indicates that, while solar radiation over other sea areas, particularly above 30°N in the North Pacific, essentially showed a decreasing trend, solar radiation over the North Atlantic showed a significant (or extremely significant) increase. In general, there is a noticeable downward trend in solar radiation over and around the equator of the North Indian and South Atlantic Oceans. Moreover, the trend is essentially declining along the west coast of South America and increasing along the coast of Southeast Asia (Figure S16b).

East Asia, South Asia, and Southeast Asia have more forests and cultivated areas compared to shrub land. Regions with the highest concentrations of urban land include eastern China, Western Europe, and the east coast of the United States (Figure S17). During the research period, urban land use exhibited the most significant change, showing a substantial increasing trend globally (Figure S18e). Concurrently, there is a noticeable decline in cropland areas in China, India, and Europe (Figure S18d).

The population is densely concentrated in India, eastern and northern China, the central plains, and southwestern Indonesia, with sporadic densely populated areas in other countries (Figure S19a). It is also evident that a significant portion of the population resides near bodies of water. Generally, populations are concentrated in coastal, lake, and riverside locations. Notable examples include the African shore of the Nile River, particularly in the northern region near the Mediterranean Sea, and the population distribution around the Great Lakes in the United States. During the research period, there was a notable decrease in population density in regions such as eastern Brazil and northern Europe, and a significant increase in densely populated areas such as India (Figure S19b).

Human footprint values are low in alpine and desert regions, such as the Sahara and areas between 60° N and 90° N. However, these values are higher near coastal and inland waters in eastern and southern Asia, western Europe, and eastern North America (Figure S20a). During the research period, the trend of human activity footprints exhibited a significant increase in most parts of the world, with only a notable decrease observed in eastern Russia and central and western Australia (Figure S20b).

Construction of Geographically and Temporally Weighted Regression

There is no significant collinearity among the explanatory variables since the GTWR model requires spatial autocorrelation of the explained events. The Moran's I index test confirms that BAA and CBD data exhibit spatial autocorrelation (Table S7), aligning with the GTWR's requirement for "spatial autocorrelation of explained variables". The GTWR model, being a linear model, necessitates that explanatory variables do not exhibit severe collinearity (VIF < 10). The collinearity test results indicate high collinearity between solar radiation, daytime and nighttime wind speeds, and SST. Factors were screened by ranking the contribution rates of GeoDetector: In open water, the BAA driving mechanism excluded solar radiation, nighttime SST, and daytime wind speed; in coastal waters, the BAA driving mechanism excluded nighttime SST and daytime wind speed; in open water, the CBD driving mechanism excluded daytime SST, nighttime SST, and daytime wind speed; in coastal waters, the CBD driving mechanism excluded nighttime SST and nighttime wind speed. A multicollinearity test was performed on the screened variables, and the results are shown in Tables S5 to S8.

The results indicate that the BAA-driven model for land coastal waters comprises daytime SST, nighttime wind speed, pH, rainfall, solar radiation, salinity, population, human footprint, and land use. For open waters, the BAA-driven model includes daytime SST, nighttime wind speed, pH, rainfall, and salinity. The CBD-driven model for land coastal waters consists of daytime SST, daytime wind speed, pH, rainfall, solar radiation, salinity, population, human footprint, and land use. The CBD-driven model for open waters includes rainfall, salinity, solar radiation, and daytime wind speed These models adhere to the GTWR requirement that "no strong collinearity exists in explanatory variables." All variables are independent and do not interfere with the model's stability due to mutual influence. Therefore, further modeling analysis is feasible.

Table S12 displays the essential parameter results of the GTWR model used in this investigation, and Figure S20 shows the results of linear fitting of the GTWR model's predicted and actual values. The R^2 values indicate that the model has a satisfactory fitting effect.

Major Driving Factors: A Spatiotemporal Regression Analysis

Temperature directly influences algal bloom development, but not all kinds of blooms have consistent temperature-growth responses globally[1]. In a majority of open seas, the regression coefficient between daytime SST and the BAA is positive, particularly in the North Atlantic and the Arabian Sea, indicating that rising temperatures have triggered blooms in these regions. Previous research has shown that the affected area of algal blooms increases with rising temperatures[1]. However, in coastal waters, the regression coefficient between daytime SST and BAA is negative (Figure S11a and Figure S11b), suggesting that higher sea surface temperatures result in smaller bloom sizes. Blooms typically appear after a certain temperature threshold is reached. When water temperatures rise beyond this threshold, the division rate of phytoplankton cells slows down or halts, eventually leading to the bloom's decline[2]. SST changes also have indirect effects on blooms; for instance, rising SST can increase ocean stratification, promoting the growth of *dinoflagellates*, which can migrate vertically to access deeper nutrients[3]. At high latitudes, stratification can isolate phytoplankton from nutrient-rich, colder upper waters[4], favoring *diatom* development over *dinoflagellates*[5]. Determining the precise net effect of SST on marine phytoplankton blooms is challenging due to the interaction between SST and other environmental factors, which often shows a significant two-factor amplification (Figure 3b).

In general, wind speed has a beneficial impact on BAA (Figures S12c and S12d), particularly in the North Atlantic and Arctic Ocean. This finding contrasts with the conventional wisdom that wind speed and algal blooms are inversely related[6]. However, the effect of wind on phytoplankton blooms largely depends on the wind's direction and the specific region it affects. Abnormally intense algal blooms can also occur during windy seasons[7]. For instance, westerly winds in the Southern Ocean carry aerosols laden with nutrients from Australian wildfires across the ocean, which are then deposited into the water by precipitation, leading to massive algal blooms[7]. Moreover, the annual average wind speed across most of the world's oceans is less than 8 $m*s^{-1}$, except in the westerly belt (Figures S12a and S12b). This suggests that lower wind speeds do not submerge algae, causing the blooms to "disappear". Instead, they actively contribute to the migration and spread of the blooms. Consequently, there are regional variations in the effect of wind speed on marine phytoplankton blooms.

The impact of solar radiation on algal bloom dynamics varies significantly across different ocean regions. In coastal areas of North and South America, the North Pacific coast, and the Eastern Atlantic coast, solar radiation has a substantial positive effect on BAA (Figures S7g and S7h) and CBD (Figures S8c and S8d). Conversely, in open waters, solar radiation exhibits a slight negative effect on the cumulative number of algal bloom days (Figures S8c and S8d). This phenomenon may be attributed to differences in water turbidity. Coastal areas often have turbid waters due to sediments such as silt carried by rivers, whereas open waters, far from land and human activities, are typically very clear. Water turbidity directly affects the penetration of solar radiation, thereby influencing light utilization by phytoplankton. Consequently, the impact of solar radiation differs markedly between coastal zones and open waters. Over time, the regression coefficients from 2003 to 2020 have remained relatively stable (Figures S8c and S8d).

In 2003, influence of salinity on BAA was primarily observed in the coastal zones of Brazil and Argentina, the southern Atlantic Ocean, and the eastern sea area of Australia. Notably, the regression coefficient between BAA and salinity showed a positive effect only in New Zealand's coastal waters (Figure S7e). By 2020, salinity impacts on BAA had increased along the eastern coast of South America and near the equator in the western Pacific Ocean (Figure S7f). The effect of salinity on CBD was also more pronounced in coastal zones, particularly along the eastern coast of South America and the northeastern coast of Asia, exhibiting negative and positive effects, respectively (Figure S8a and Figure S8b). Over time, significant changes were observed in the North Pacific Ocean: Salinity had a weak positive effect on bloom CBD in 2003 (Figure S8a) but a negative effect in 2020 (Figure S8b). Overall, salinity's negative impact on bloom dynamics is more significant in coastal zones, suggesting that intensified water circulation due to climate change[8] and large groundwater discharges[9] reduce coastal seawater salinity while enriching coastal ecosystems with nutrients, leading to increased blooms. For blooms more adaptive to high salinity environments (e.g., *Trichodesmium*[10]), the effect of salinity on bloom dynamics shows a positive impact in waters with high net evaporation and salinity.

The coastal zone of South Africa and the area near the North Pacific Ocean are regions where precipitation significantly impacts the CBD. These areas generally exhibit negative effects, while other sea areas show no readily apparent control effect (with regression coefficients between -2 and 2) (Figures S8e and S8f). This indicates that periods of heavy precipitation limit phytoplankton biomass[11]. The strength of precipitation largely determines its impact on algal blooms. As precipitation intensity increases, the degree of algal blooms generally decreases. Thus, increased rainfall usually restricts the overall duration of algal blooms. However, in 2020, precipitation positively affected CBD along the northeast Asian coast. This suggests that increased precipitation may enhance the nutrient load of estuaries, creating favorable hydrological conditions for phytoplankton growth, thereby increasing the likelihood of blooms in continental coastal zones[12].

Methods for Collinearity Analysis

To evaluate the presence and severity of multicollinearity among the explanatory variables, we employed Variance Inflation Factor (VIF) analysis. VIF quantifies the extent to which the variance of an estimated regression coefficient is inflated due to linear dependence among predictors[13]. It is computed as:

$$\mathrm{VIF_i} = \frac{1}{1-\mathrm{R_i^2}} \quad (1)$$

where $\mathrm{R_i^2}$ is the coefficient of determination obtained by regressing the ith predictor against all other predictors in the model. A VIF value exceeding 10 is interpreted as evidence of moderate to severe multicollinearity.

In this study, VIF values were computed for all explanatory variables prior to interaction analysis in the geographic detector model. While the geographic detector's single-factor (q-value) is unaffected by multicollinearity[14], high VIFs (>10) between paired variables (e.g., DSST-NSST) imply that their interaction terms may overestimate joint effects (see Table S1).

Methods for Granger Causality Analysis

Granger causality is a statistical method used to test whether one time series provides predictive information about another[15]. If past values of variable X significantly improve the forecast of variable Y beyond Y's own history, X is said to Granger-cause Y. This approach compares two models: a restricted model using only Y's lagged terms and an unrestricted model incorporating lagged values of both X and Y.

$$\begin{cases} Y_t = \sum_{i=1}^{m} \beta_i Y_{t-i} + \varepsilon_t & \text{(redeced model)} \\ Y_t = \sum_{i=1}^{m} \beta_i Y_{t-i} + \sum_{i=1}^{m} \gamma_i X_{t-i} + \varepsilon_t & \text{(full model)} \end{cases} \quad (2)$$

where t represents a given point in time; β_i and γ_i represent regression coefficients for previous time i; ε_t represents an error term; m is the lag.

A significant reduction in residual variance when including X indicates a causal link. Implemented within a vector autoregression (VAR) framework, the test typically employs an F-statistic:

$$F = \frac{(RSS_R - RSS_F)/l}{RSS_F/(t-r)} \tag{3}$$

Here, RSS_r and RSS_f represent the residual sum of squares from the reduced and full models, respectively. Using this test, X is declared Granger causal for Y if the observed test statistic F exceeds the (1 - α)% quantile of an F-distribution with l and $t - r$ degrees of freedom.

Supplementary figures

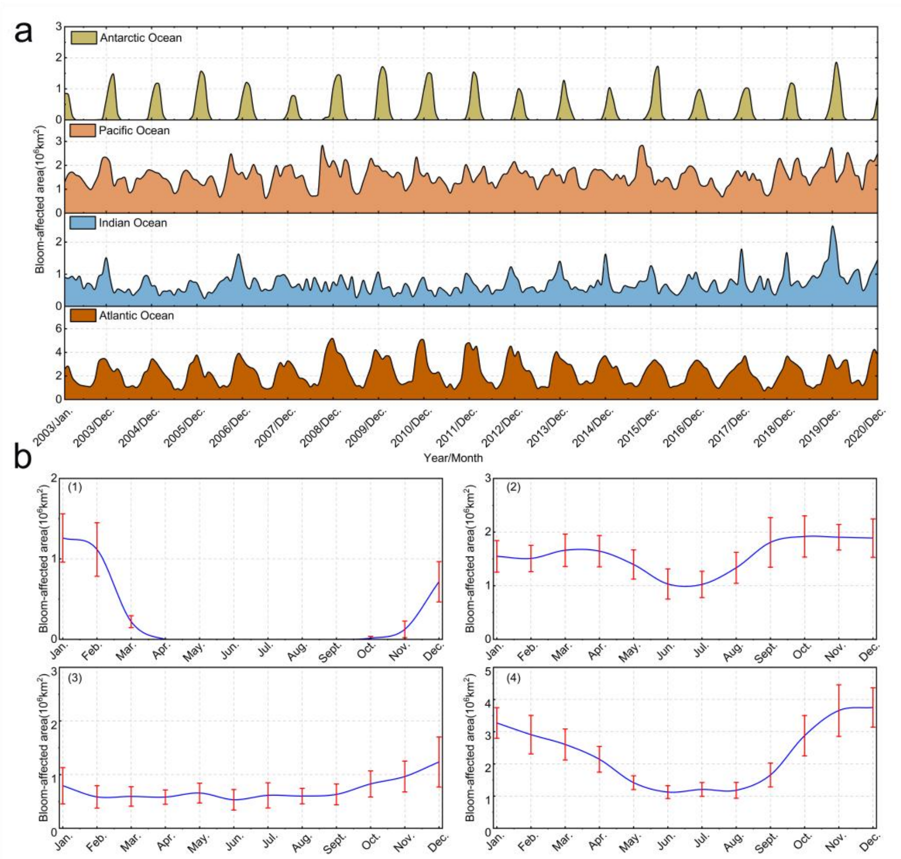

Figure S1 Monthly trends in algal bloom area in the four major oceans of the Southern Hemisphere. **a** presents the annual changing trend of BAA in the Southern Hemisphere's four main seas. The green section represents the Antarctic Ocean bloom. The orange section depicts the South Pacific bloom. The blue section represents the South Indian Ocean bloom. The brown area shows the South Atlantic algal bloom. **b** illustrates the multi-year average monthly scale annual change trend of the algal bloom area in the four Southern Hemisphere oceans. **b (1),** The Antarctic Ocean trend. **b (2),** The South Pacific Ocean trend. **b (3),** The South Indian Ocean trend. **b (4),** The South Atlantic Ocean trend. The sample standard deviation in **b** is indicated by the red error bars.

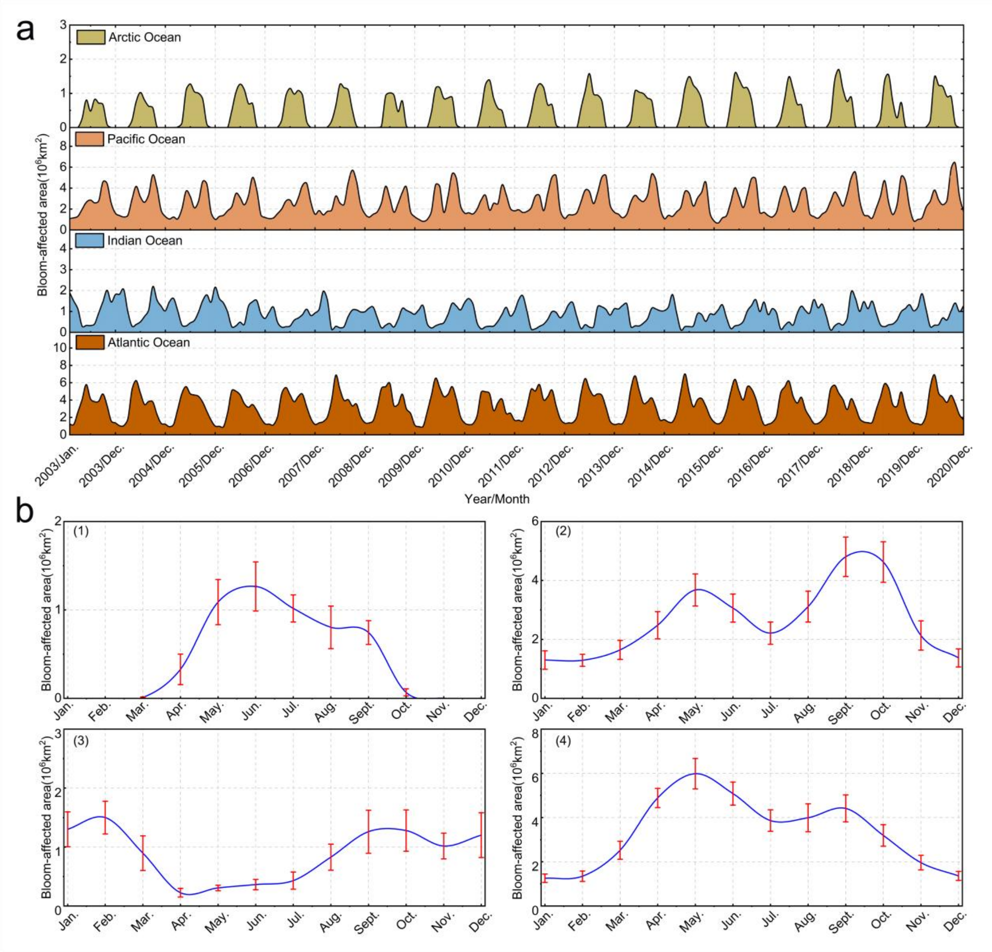

Figure S2 Monthly trends of BAA in the four major oceans of the Northern Hemisphere. a, The annual changing trend in BAA across the four main seas of the Northern Hemisphere. The green area represents the Arctic Ocean bloom. The orange area depicts the North Pacific bloom. The blue area represents the North Indian Ocean bloom. The brown area indicates the North Atlantic bloom. **b**, The annual trend of the multi-year average monthly scale of BAA in these oceans. **b (1),** The Arctic Ocean trend. **b (2),** The North Pacific Ocean trend. **b (3),** The North Indian Ocean trend. **b (4),** The North Atlantic Ocean trend. The red error bars in **b** indicate the sample standard deviation.

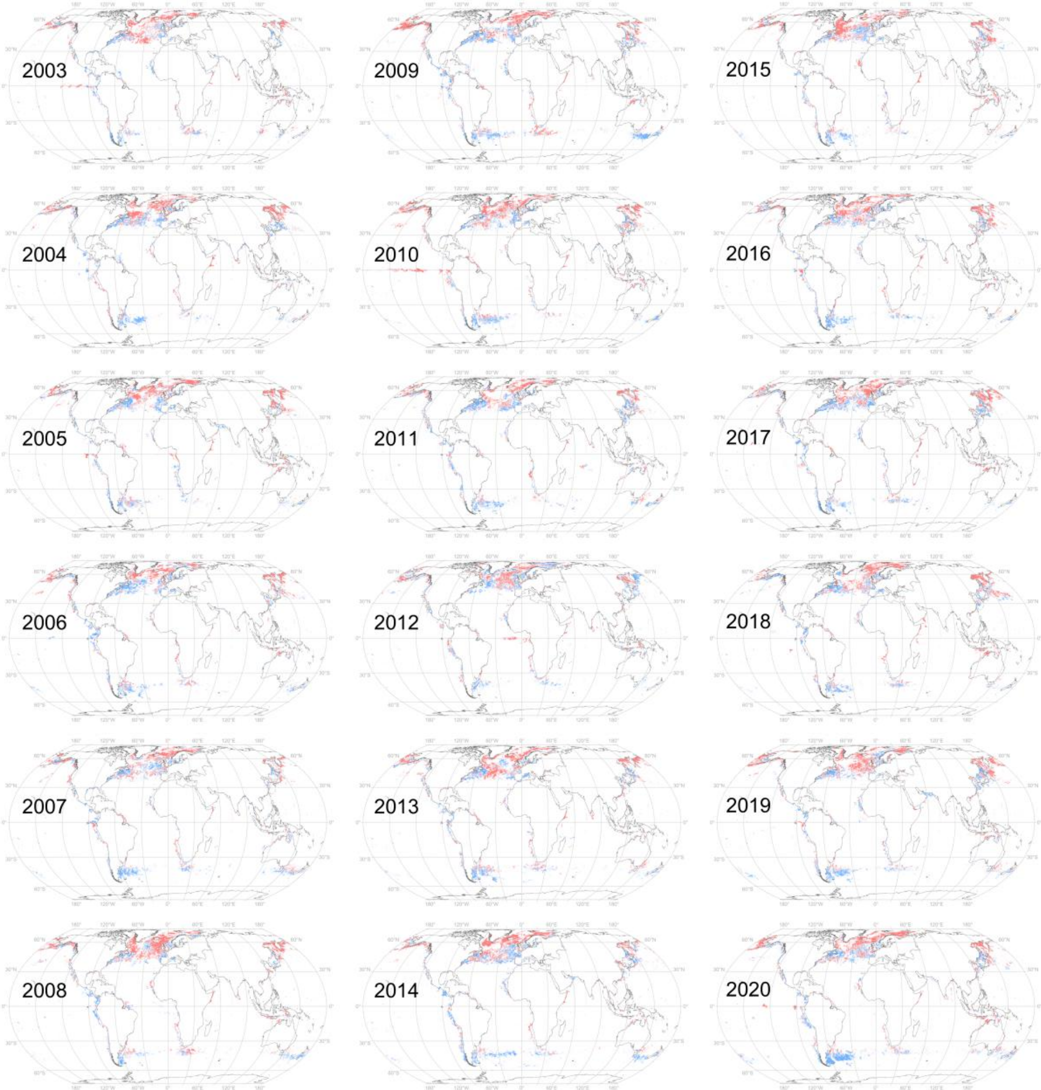

Figure S3 Trend chart of the global marine algal bloom area during the 'first peak' from 2003 to 2020. The red regions indicate areas where new algal blooms emerged during the peak month compared to the previous month, and the blue regions indicate areas where algal blooms declined. The increase in algal blooms during the first peak month is primarily concentrated in the North Atlantic and North Pacific.

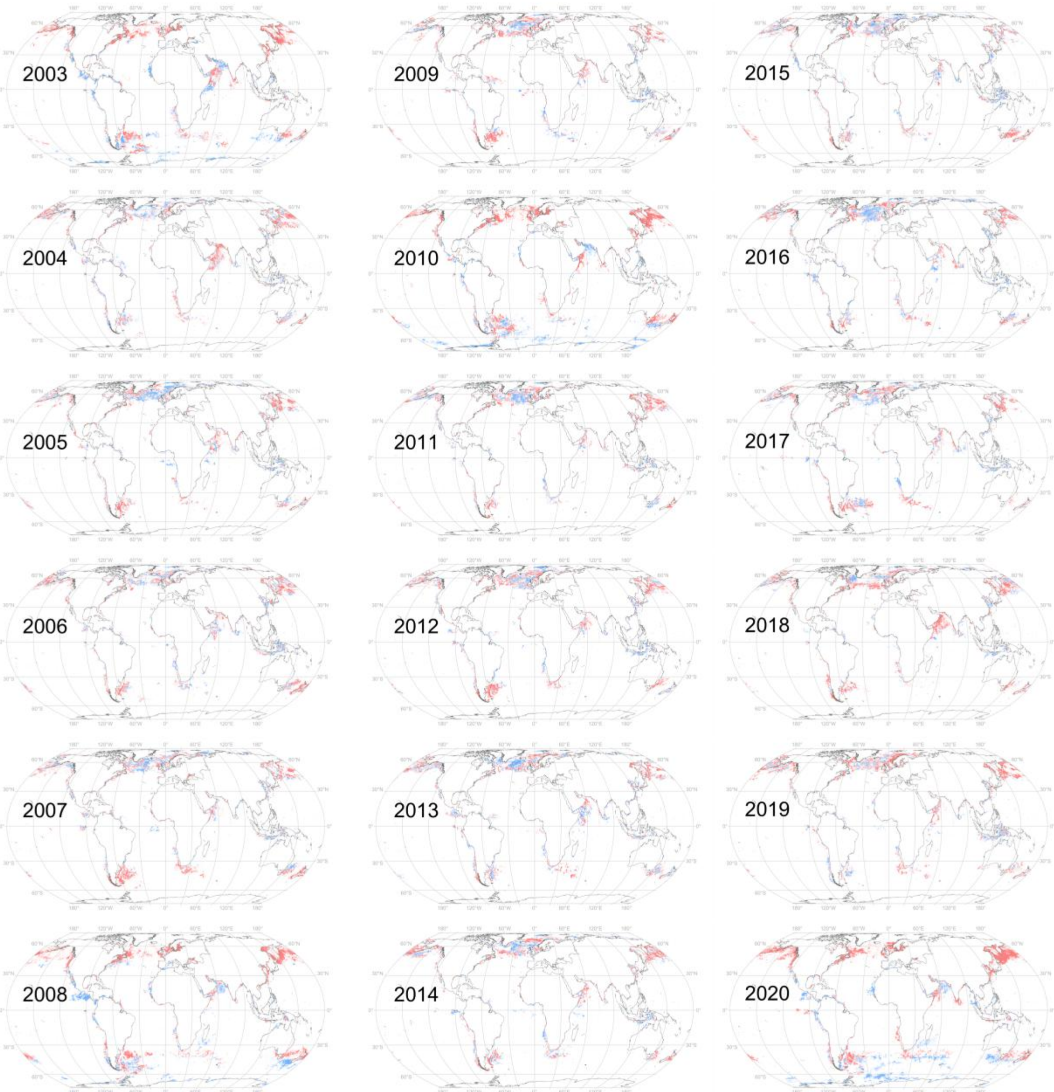

Figure S4 Trend chart of the global marine algal bloom area during the 'second peak' from 2003 to 2020. The red regions indicate areas where new algal blooms emerged during the peak month compared to the previous month, and the blue regions indicate areas where algal blooms declined. The increase in algal blooms during the second peak month is primarily concentrated in the North Pacific.

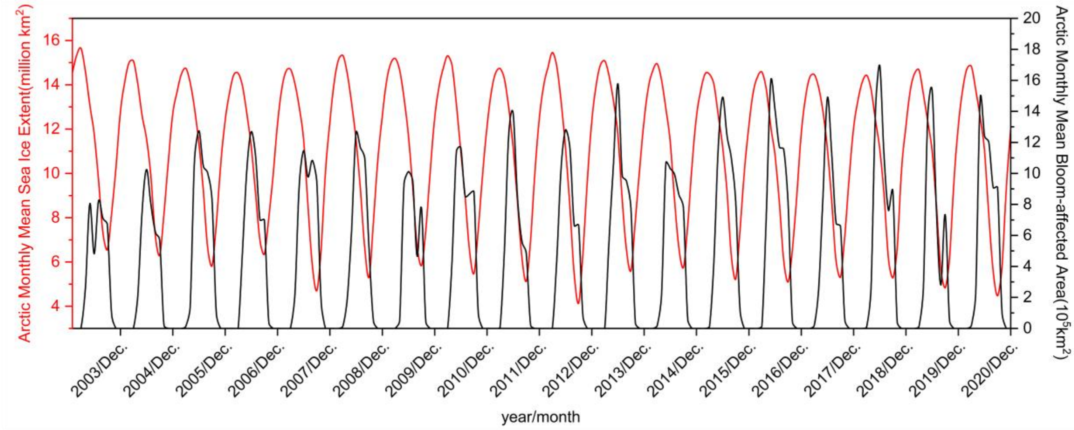

Figure S5 Monthly trend of BAA and sea ice in the Arctic Ocean. The monthly variations in the sea ice extent of the Arctic Ocean are depicted by the red line. The sea ice extent reaches its maximum in March and then progressively decreases as the temperature rises, reaching its minimum in September before it begins to grow again. BAA by Arctic Ocean is represented by a black line, illustrating monthly variations.

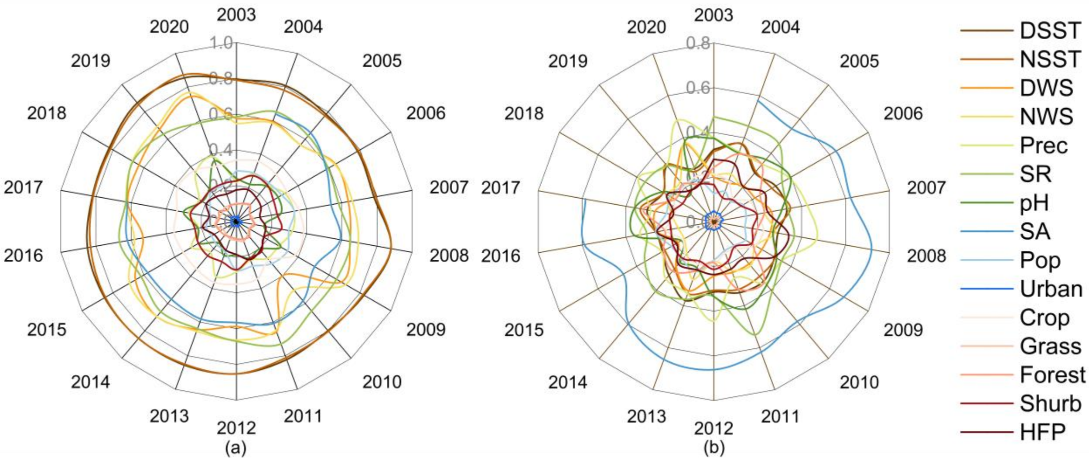

Figure S6 Contribution degree of each environmental factor to algal blooms. The contribution of each environmental element to algal blooms (i.e., the q value result of the factor detection function of the geographical detector) is analyzed based on units of 0.1° latitude, with n=1800. The factor detection q-value findings for each environmental factor on the BAA are displayed in **a**, and those for CBD are displayed in **b**. Salinity and sea surface temperature have the most significant effects on both CBD and BAA.

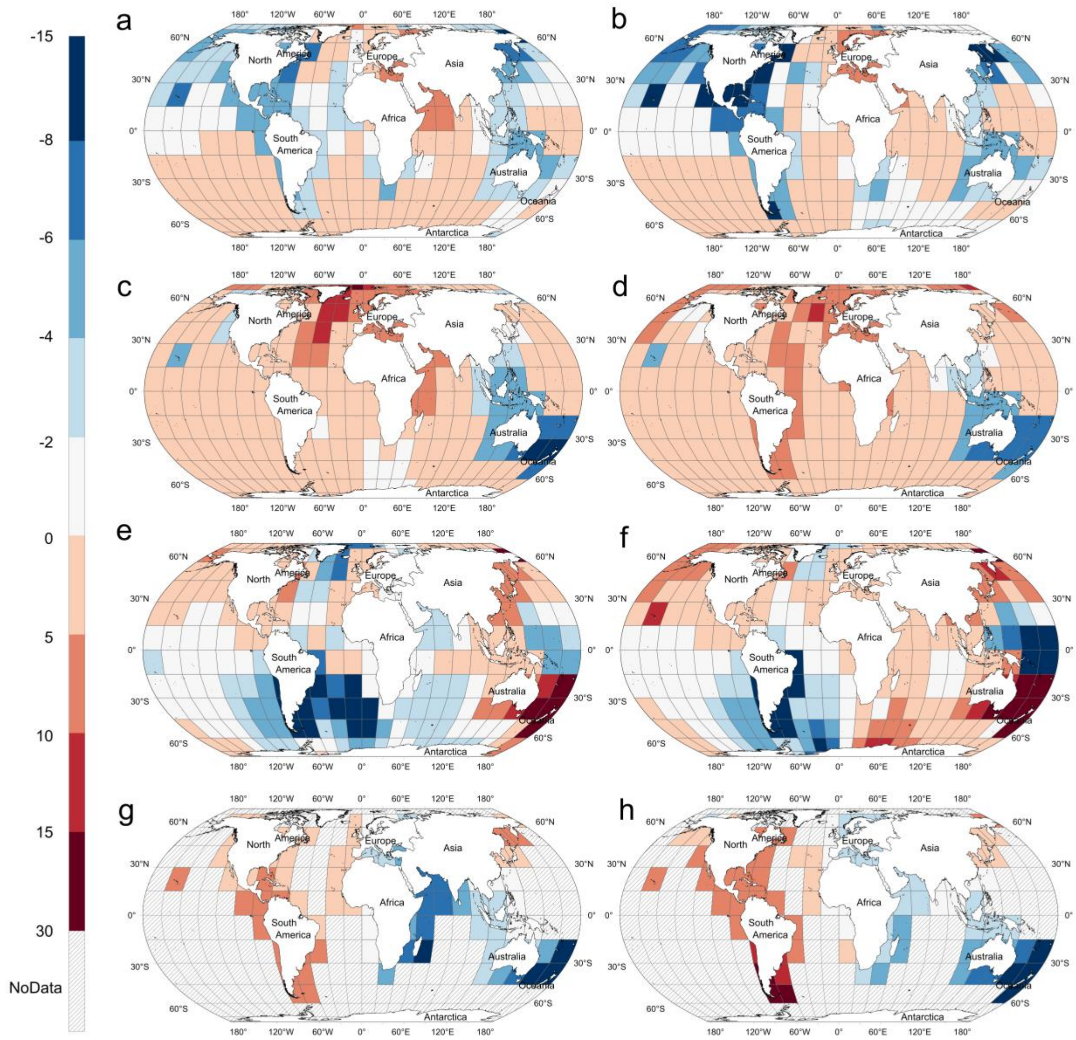

Figure S7 Spatial distribution of regression coefficients for the main influencing factors on phytoplankton bloom-affected areas. **a**, Regression coefficients for daytime SST in 2003. **b**, Regression coefficients for daytime SST in 2020. **c**, Regression coefficients for nighttime wind speed in 2003. **d**, Regression coefficients for nighttime wind speed in 2020. **e**, Regression coefficients for salinity in 2003. **f**, Regression coefficients for salinity in 2020. **g**, Regression coefficients for solar radiation in 2003. **h**, Regression coefficients for solar radiation in 2020.

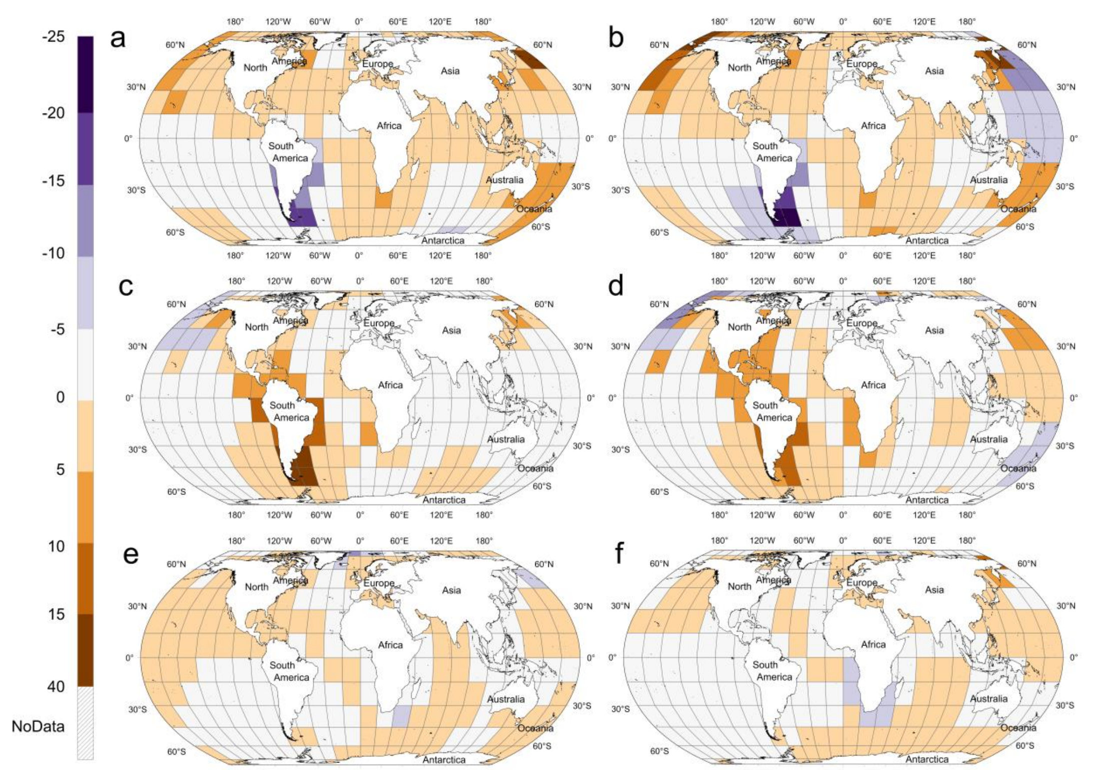

Figure S8 Spatial distribution of regression coefficients for the main influencing factors on cumulative days of phytoplankton bloom. Regression coefficients for **a**, salinity in 2003. **b**, salinity in 2020. **c**, solar radiation in 2003. **d**, solar radiation in 2020. **e**, precipitation in 2003. **f**, Regression precipitation in 2020.

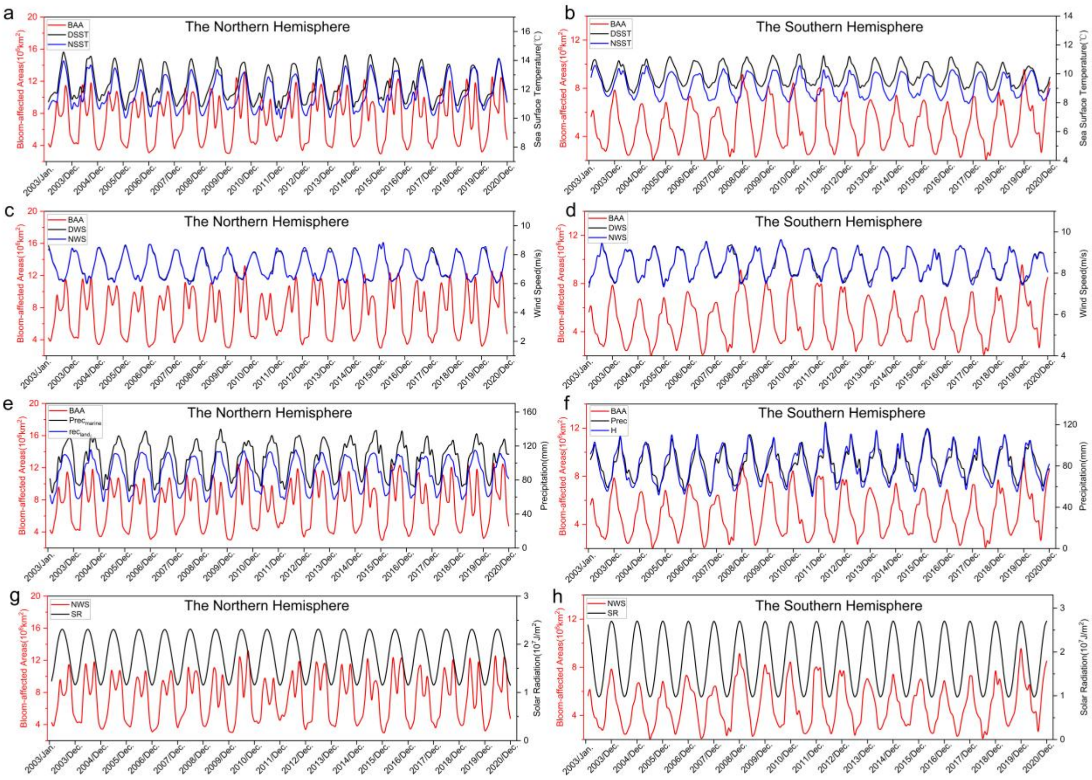

Figure S9 Monthly variation in climatic elements and BAA (a), (c), (e), and (g) represent BAA and climate elements in the Northern Hemisphere, and (b), (d), (f), and (h) represent BAA and climate elements in the Southern Hemisphere.

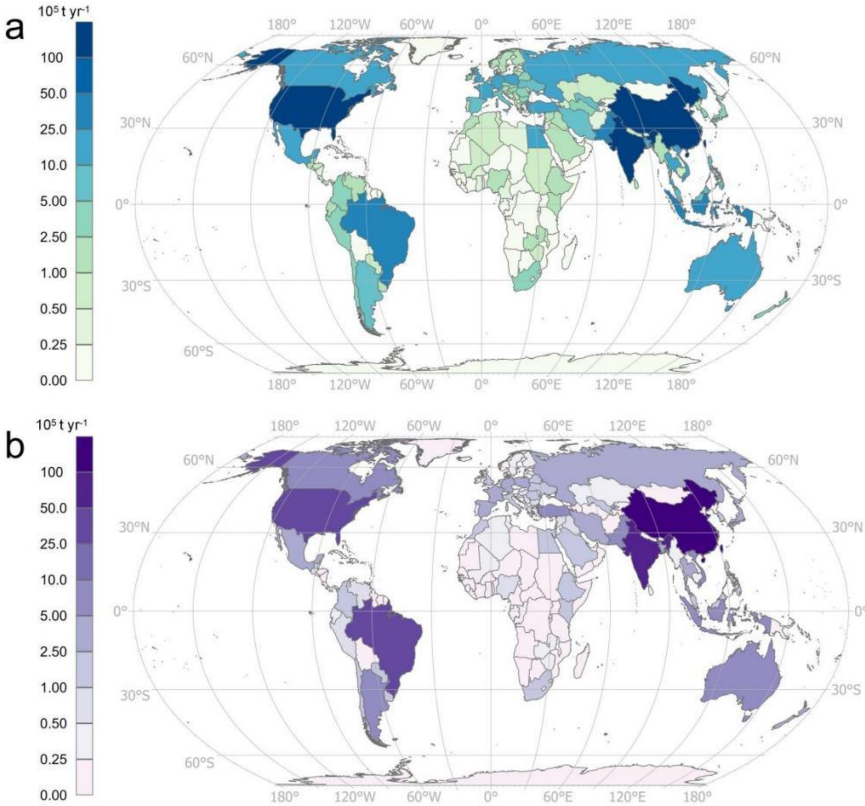

Figure S10 Annual average nitrogen and phosphorus fertilizer application in agriculture. a, Annual average application of agricultural nitrogen fertilizer. **b,** Annual average application of agricultural phosphate fertilizer. Higher amounts of fertilizer application are indicated by lighter hues. Countries with the highest fertilizer usage include Brazil, China, India, and the United States.

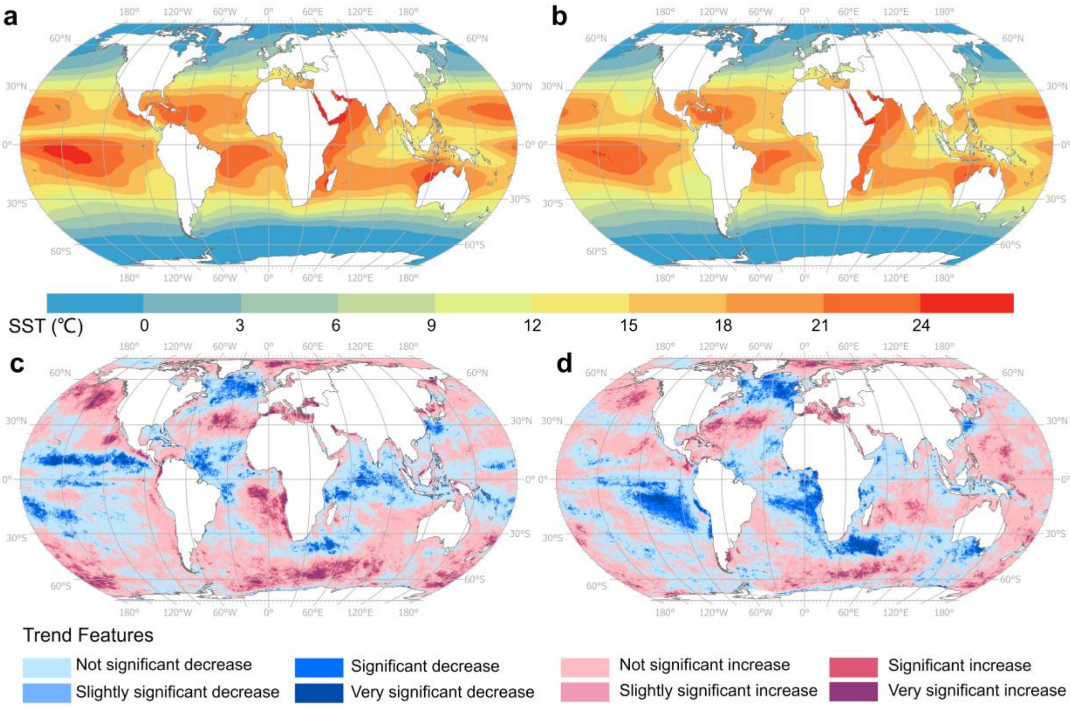

Figure S11 Average annual SST and its changing trends from 2003 to 2020. Daytime temperature and its variation trend are depicted in **a** and **c** and nighttime temperature and its variation trend in **b** and **d**. The impact of wind and ocean currents prevents the temperature of the ocean's surface from displaying a latitude distribution. Certain open seas and certain coastal waters have warmer sea surface temperatures.

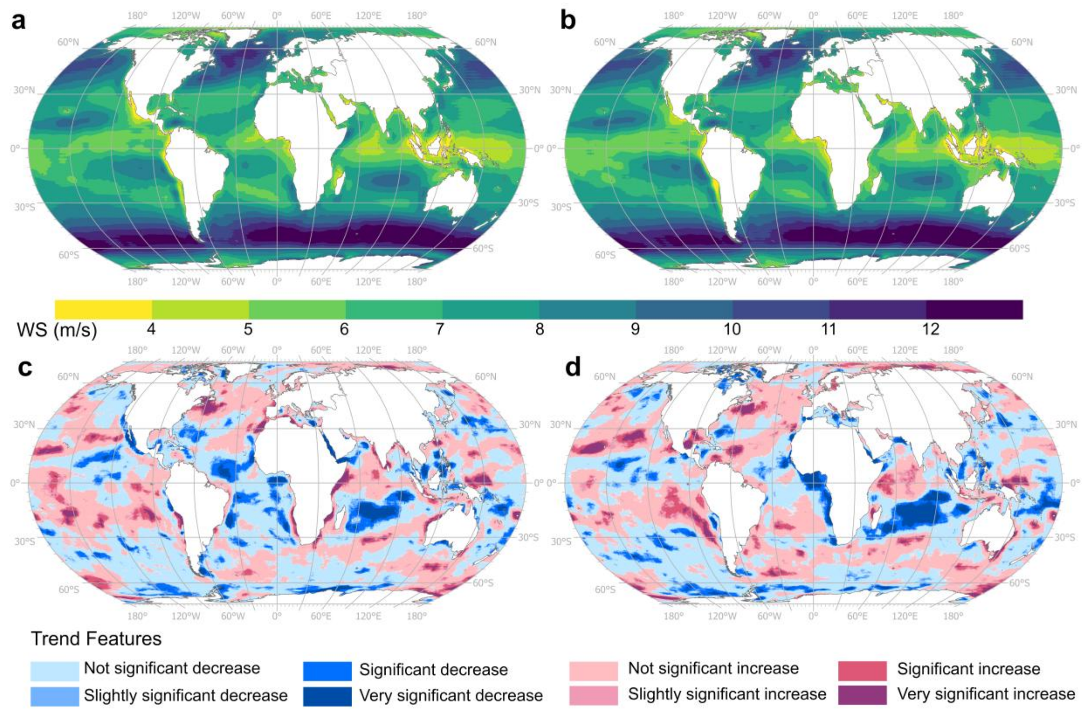

Figure S12 Average annual wind speed and its changing trends from 2003 to 2020. Daytime wind speed and its variation trend are depicted in **a** and **c**; nighttime wind speed and its variation trend are shown in **b** and **d**. The westerly belt is the strongest wind zone in the world.

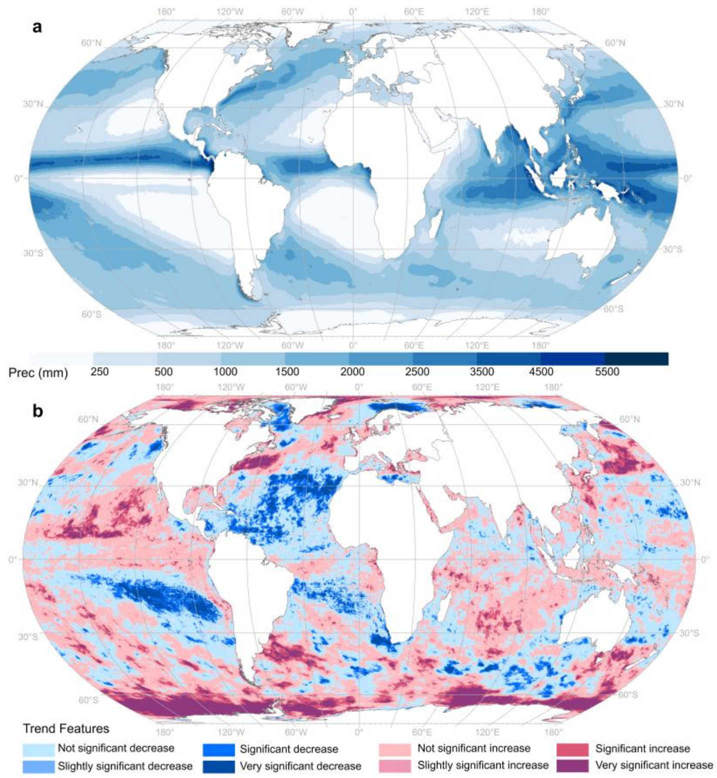

Figure S13 Average annual total precipitation and its changing trends from 2003 to 2020.

Average annual total precipitation is depicted in **a** and its variation trend in **b.** The equatorial rain belt is the location of the global maximum rainfall, with comparatively large rainfall near the equator. Similarly, the temperate rain belt experiences relatively large rainfall, with clear deviations due to monsoon influence. Overall, global rainfall exhibited and upward trend during the study period.

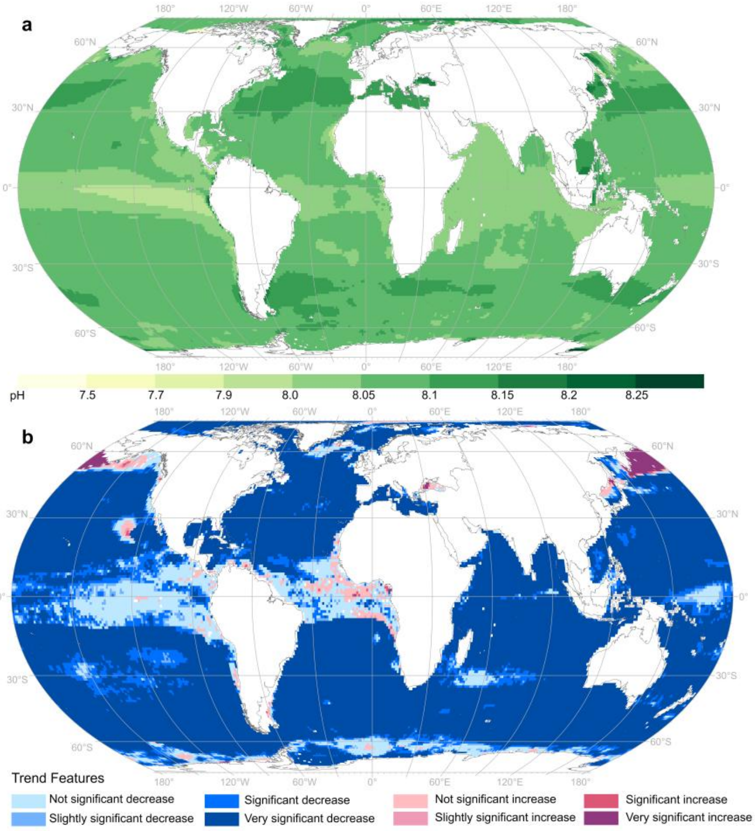

Figure S14 Average annual pH and its changing trend of the sea surface (0 m) from 2003 to 2020. Average annual pH depicted in **a** and its variation trend in **b.** Near the equator, the worldwide ocean pH value is lower. During the research period, pH drastically decreased and exhibited clear signs of acidification.

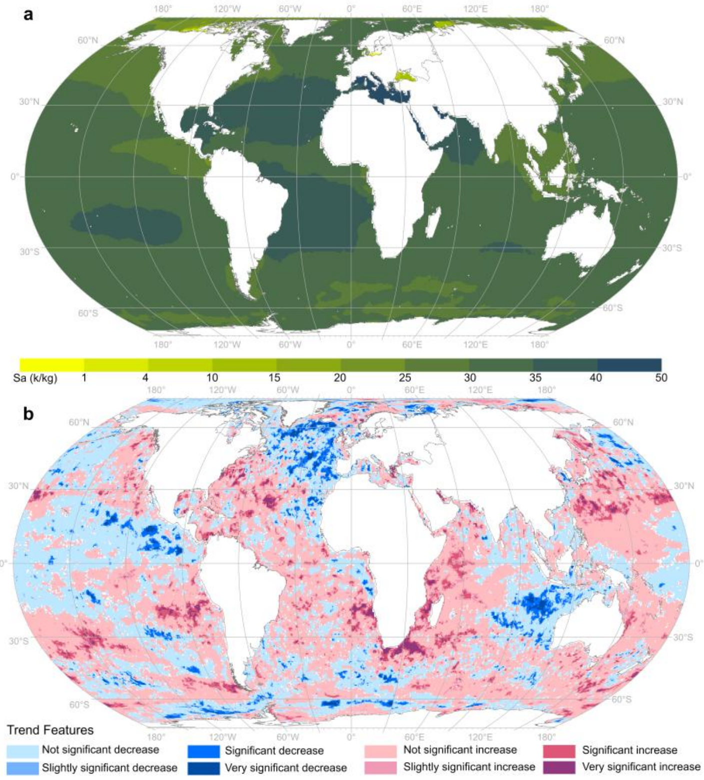

Figure S6 Average annual salinity and its changing trend of the sea surface (0 m) from 2003 to 2020. Average annual salinity depicted in **a** and its variation trend in **b.** Salinity is higher in the middle and low latitudes of the Atlantic Ocean, and, generally, salinity changes show an increasing trend.

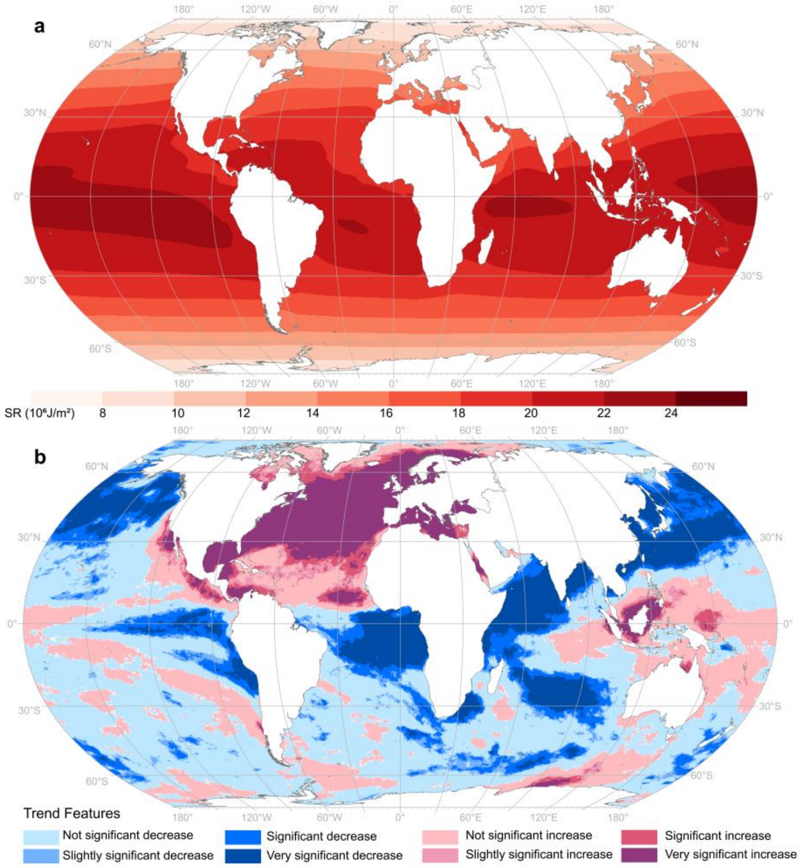

Figure S7 Average annual solar radiation from 2003 to 2020 and its changing trend. Average annual solar radiation depicted in **a** and its variation trend in **b.** Yearly solar radiation distribution worldwide exhibits a very significant increase in the North Atlantic Ocean and a very significant decrease in the North Pacific Ocean, with latitude running parallel to the distribution.

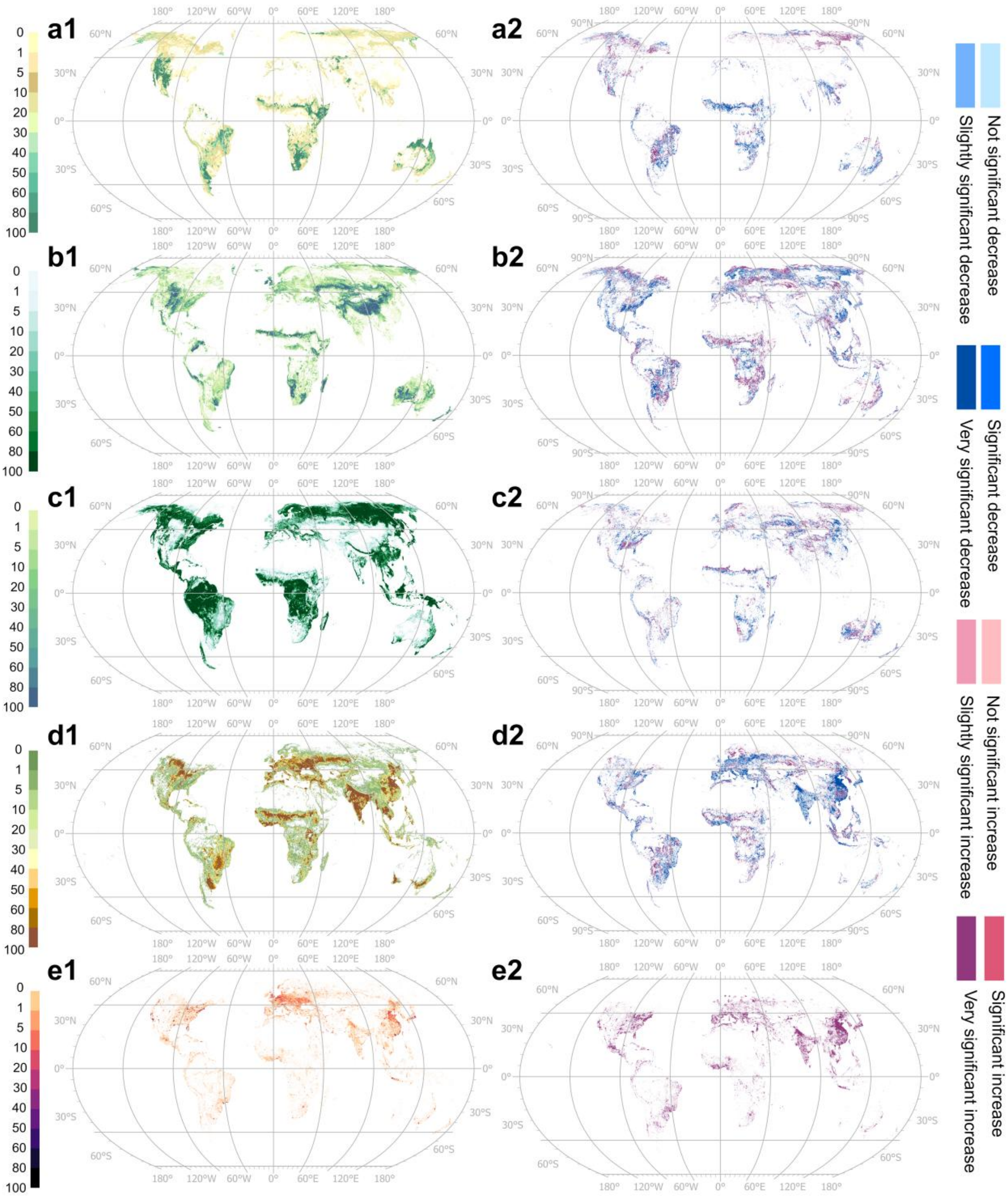

Figure S8 Average annual proportion of different land use types from 2003 to 2020 and its changing trend. a, Shrub. **b,** Grass. **c,** Forest. **d,** Crop. **e,** Urban.

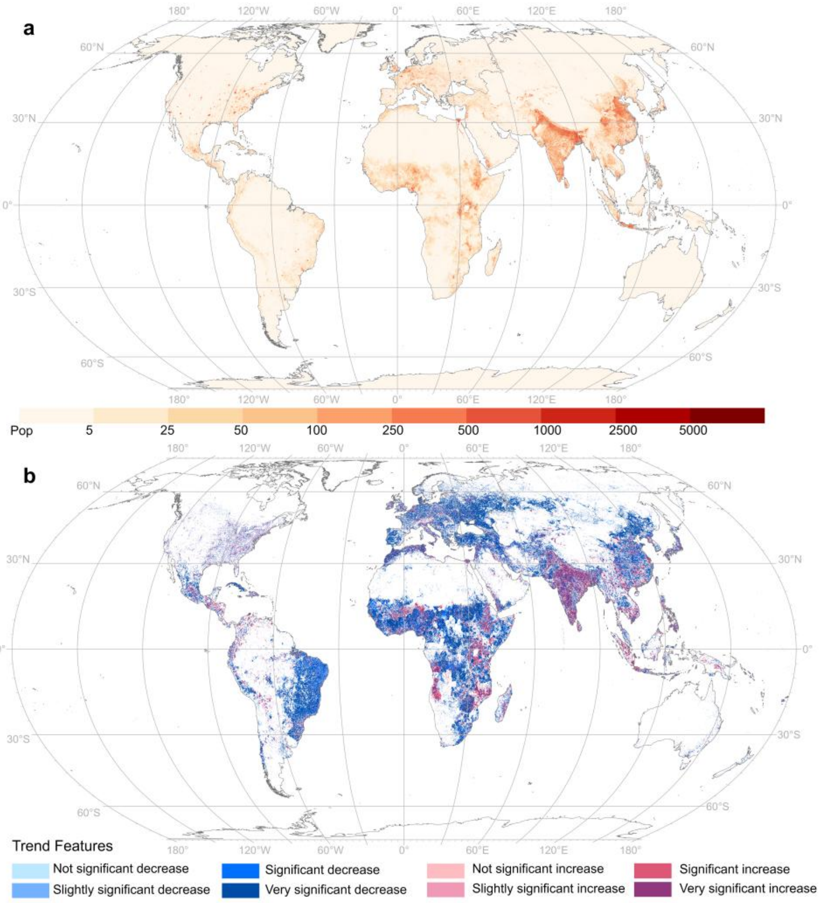

Figure S18 Average annual ambient population from 2003 to 2020 and its changing trend. Average annual ambient population is depicted in **a** and its variation trend in **b.** The population is densely distributed in India, eastern and northern China, the central plains, and southwestern Indonesia. There are sporadic densely populated areas in other countries, and most of these have also shown an increasing trend.

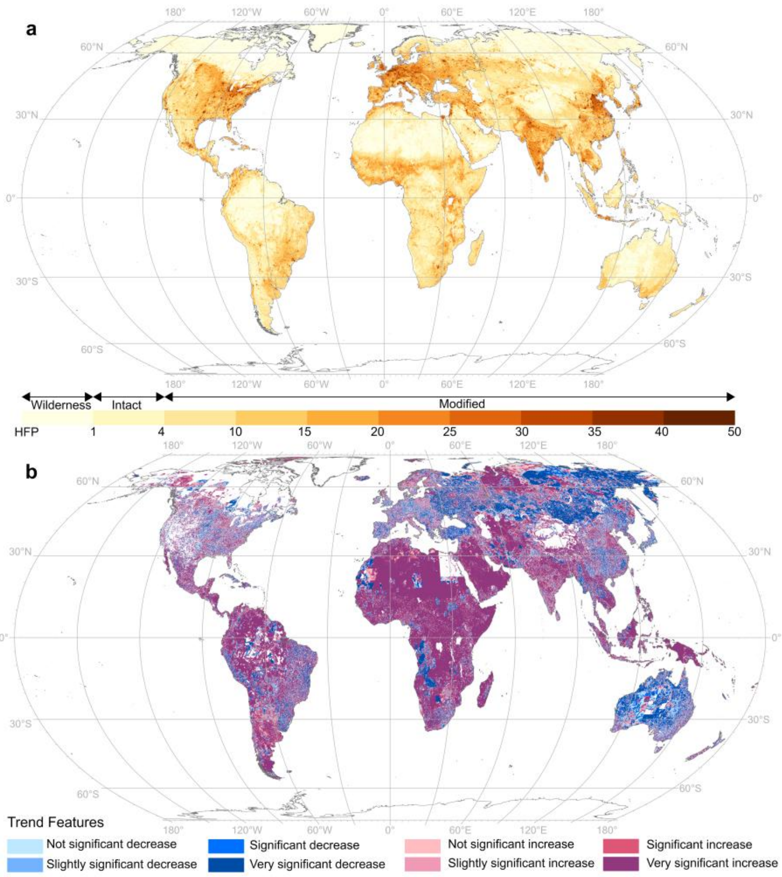

Figure S19 Average annual human footprint project from 2003 to 2020 and its changing trend. Average annual human footprint project depicted in **a** and its variation trend in **b**. The footprints of human activities are higher in areas near coastal and inland waters than in alpine and desert areas, where the footprints are sparse.

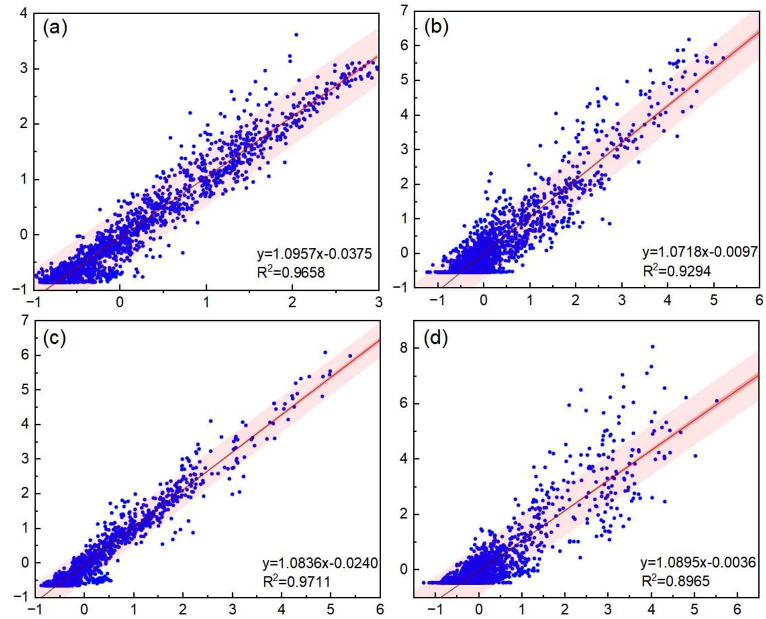

Figure S20 Results of linear fitting of the GTWR model's predicted and actual values. The linear fitting results of the GTWR model's predicted and actual values shown for different regions and metrics of algal blooms: a, Model fitting results for the area affected by algal blooms in coastal zones. b, Model fitting results for the area affected by algal blooms in open waters. c, Model fitting results for the cumulative number of days of algal blooms in coastal zones. d, Model fitting results for the cumulative number of days of algal blooms in open waters.

Table S1 Correlation and multicollinearity analysis of variables

	DSST	NSST	DWS	NWS	Prec	SR	pH	Pop	Urban	Crop	Grass	Forest	Shurb	HFP
DSST	-	**747.86**	1.44	1.48	1.51	7.84	1.13	1.24	1.19	1.76	1.31	1.39	1.77	1.7
NSST	**0.999**	-	1.44	1.47	1.51	7.5	1.13	1.25	1.18	1.74	1.3	1.37	1.74	1.68
DWS	-0.552	-0.552	-	**448.12**	1.02	1.09	1.05	1.14	1.07	1.2	1.06	1.2	1.06	1.08
NWS	-0.568	-0.567	**0.999**	-	1.03	1.11	1.06	1.14	1.07	1.2	1.07	1.21	1.07	1.09
Prec	0.583	0.581	-0.144	-0.162	-	2.17	1.14	1.05	1.11	1.25	1.24	1.76	1.6	1.58
SR	**0.934**	**0.931**	-0.288	-0.308	0.734	-	1.13	1.13	1.2	1.66	1.37	1.43	2.16	1.88
pH	-0.343	-0.341	0.226	0.234	-0.346	-0.343	-	1.02	1	1.01	1	1.22	1.01	1
Pop	0.442	0.447	-0.354	-0.352	0.211	0.34	0.138	-	1.42	1.49	1.29	1.06	1.07	1.64
Urban	0.397	0.39	-0.248	-0.252	0.312	0.407	0.051	0.545	-	1.57	1.39	1.14	1.2	1.81
Crop	0.658	0.653	-0.405	-0.409	0.448	0.63	-0.073	0.575	0.604	-	1.26	1.2	1.23	4.18
Grass	0.486	0.479	-0.24	-0.249	0.437	0.519	0.027	0.477	0.531	0.452	-	1.13	1.51	1.89
Forest	0.531	0.519	-0.408	-0.416	0.657	0.548	-0.424	0.237	0.354	0.412	0.334	-	1.25	1.22
Shurb	0.659	0.652	-0.24	-0.256	0.611	0.733	-0.092	0.258	0.409	0.429	0.58	0.445	-	1.55
HFP	0.641	0.637	-0.274	-0.282	0.607	0.683	0.02	0.624	0.669	0.872	0.687	0.424	0.596	-

Note: Lower triangle shows Pearson correlation coefficients; upper triangle displays variance inflation factors (VIF). Bold values highlight $|r| > 0.9$ or VIF > 10, indicating high multicollinearity. Diagonal cells (variable self-correlation) are omitted. All correlations are significant at $p < 0.01$ (two-tailed).

Table S2 Granger causality analysis results for the relationships between different parameters

Causal linkage (null hypothesis)	Northern Hemisphere		Southern Hemisphere	
	p value	*F* value	*p* value	*F* value
H_1	<0.001	46.45	<0.001	27.01
H_2	<0.001	44.28	<0.001	31.74
H_3	<0.001	4.55	<0.001	25.13
H_4	<0.001	4.40	<0.001	21.70
H_5	<0.001	6.92	<0.001	27.70
H_6	<0.001	6.22	<0.001	32.53
H_7	<0.001	13.76	<0.001	33.94

Note: H_1: Daytime sea surface temperature does not Granger-cause with marine phytoplankton bloom patterns, H_2: Nighttime sea surface temperature does not Granger-cause with marine phytoplankton bloom patterns, H_3: Daytime windspeed does not Granger-cause with marine phytoplankton bloom patterns, H_4: Nighttime windspeed does not Granger-cause with marine phytoplankton bloom patterns, H_5: Marine precipitation does not Granger-cause with marine phytoplankton bloom patterns, H_6: Land precipitation does not Granger-cause with marine phytoplankton bloom patterns, H_7: Solar radiation does not Granger-cause with marine phytoplankton bloom patterns.

Table S3 The top 30 algae bloom-dominant species and their main distribution countries in HAEDAT

Rank	Causative species name	Major country	Count	Secondary country	Count	Total
1	*Pyrodinium bahamense*	Philippines	955	United States	27	1064
2	*Dinophysis acuminata*	Spain	380	Portugal	281	1037
3	*Dinophysis spp.*	France	332	United Kingdom	111	830
4	*Alexandrium*	Norway	208	United States	159	594
5	*Pseudo-nitzschia*	United States	143	France	135	573
6	*Dinophysis acuta*	Norway	133	Portugal	108	384
7	*Gymnodinium catenatum*	Portugal	132	Spain	93	334
8	*Alexandrium catenella*	United States	171	Chile	46	329
9	*Nodularia spumigena*	Sweden	133	Poland	56	240
10	*Alexandrium tamarense*	Norway	62	Canada	33	189
11	*Skeletonema costatum*	France	93	China	34	185
12	*Margalefidinium polykrikoides*	Korea	56	Japan	25	164
13	*Chaetoceros*	France	79	Portugal	21	146
14	*Pseudo-nitzschia australis*	Spain	106	Portugal	15	139
15	*Karenia mikimotoi*	Japan	77	China	16	138
16	*Heterosigma akashiwo*	Canada	52	Japan	24	137
17	*Alexandrium minutum*	Spain	39	Slovenia	31	134
18	*Noctiluca scintillans*	China	21	Indonesia	16	128
19	*Dinophysis caudata*	Slovenia	31	Spain	28	126
20	*Dinophysis sacculus*	France	49	Slovenia	24	109
21	*Prorocentrum minimum*	United States	34	France	9	94
22	*Gymnodinium*	France	37	Portugal	10	82
23	*Karenia brevis*	United States	64	Mexico	11	80
24	*Phaeocystis*	France	29	Netherlands	28	75
25	*Dinophysis norvegica*	Norway	30	Canada	22	70
26	*Prorocentrum micans*	Portugal	15	Mexico	9	69
27	*Prorocentrum*	China	24	France	15	67
28	*Leptocylindrus danicus*	Portugal	31	Spain	17	56
29	*Aureococcus anophagefferens*	United States	46	South Africa	6	55
30	*Lingulodinium polyedra*	Slovenia	34	Portugal	7	54

Table S4 Detailed metadata of global harmful algal bloom events derived from HAEDAT and literature review

Species	Region/Country	Latitude/Longitude (Approximately)	Hemisphere	Years	References
Pyrodinium bahamense	Southeastern Gulf of Mexico - coast of the state of Campeche, Mexico; Philippine coastal bays and estuaries; Malaysia (Sabah, Borneo); Indonesia; Yemen; Mexico; United States; Central America; Latin America; Red Sea / Arabian / Gulf region; Yemen / Gulf of Aden / Djibouti	~ 18°N–22°N, ~ 90°W–95°W; ~8°N–13°N; ~5°N–6°N; ~6°S–5°N; ~14° 47′ 07" N, 42° 56′ 46.31" E; ~27.5°–28°N, ~82.5°W; Costa Rica (Gulf of Nicoya, Gulf of Panama), El Salvador coastal waters; ~16°–22°N	Northern Hemisphere; Northern & Southern	September and November 2016; 2003–2020; ongoing recurrent blooms; 2012–2013; 2010; 2008–2010; 2013	https://www.ncbi.nlm.nih.gov/pmc/articles/PMC9694361/; https://doi.org/10.1016/j.hal.2020.101776; https://doi.org/10.1016/j.toxicon.2009.09.017; https://doi.org/10.46754/jssm.2022.07.011; https://www.researchgate.net/publication/324942069_Occurrence_of_Pyrodinium_bahamense_blooms_related_to_cyst_accumulation_in_the_bottom_sediments_in_the_bays_at_Ambon_Lampung_and_Jakarta_Indonesia; http://doi.org/10.4194/1303-2712-v16_2_07; https://doi.org/10.3390/toxins14110760; https://doi.org/10.37543/oceanides.v28i1.122; https://www.researchgate.net/publication/265244658_The_distribution_of_Pyrodinium_bahamense_cysts_in_Old_Tampa_Bay_sediments; https://doi.org/10.2984/1534-6188(2007)61[289:FROVCO]2.0.CO;2; https://doi.org/10.30955/gnj.005388; https://doi.org/10.3389/fmars.2019.00042; https://doi.org/10.1016/j.hal.2016.03.002; https://doi.org/10.1080/09670262.2024.2447871
Karenia spp.	Gulf of Mexico; Southwest coast Florida; West Florida Shelf; Coastal seas of China; Coastal waters off the Kamchatka Peninsula; Chile, New Zealand, Mexico,	~ 25–30° N, ~ 82–86° W; ~25°–27°N, ~82°–83°W; ~24°–30°N, ~81°–87°W; lat range 18.29°N – 39.85°N;	Northern; Northern + Southern (Both)	2003–2019; 2005; 1950s–2005; 2020; 2000s–2020; 1985–2019; 2016	https://doi.org/10.1016/j.hal.2022.102289; https://doi.org/10.1016/j.hal.2008.04.008; https://doi.org/10.1016/j.hal.2006.08.005; https://doi.org/10.1016/j.hal.2021.102121; https://doi.org/10.1016/j.hal.2022.102337; https://doi.org/10.1016/j.hal.2020.101892;

	Tunisia, Kuwait, Iran, China; Australia & New Zealand; Western English Channel / Bay of Biscay	~ 50–55° N, ~160–165° E; Chile (~36–42°S, 72–76°W); Australia: ~12°–44°S; ~48°–50°N, ~-3°–2°W			https://doi.org/10.1016/j.hal.2020.101848; https://doi.org/10.1016/j.hal.2015.11.005
Pseudo-nitzschia australis	USA West Coast; California Current; Northern Gulf of Mexico; Puget Sound; North Sea / Southern Bight; Northern Patagonian shelf; Todos Santos Bay; West Coast of USA	32°–49°N, 125°–117°W; ~30°–31°N, ~87°–88°W; ~47°–49°N, ~122°–123°W; ~48°–52°N, ~1°W–4°E; ~40°–46°S, ~61°–66°W; ~31.8°N, ~116.6°W	Northern	2015–2016; 2009; 2003–2018; 1990s–2020; 2012; 2003–2017; 2008-2009	https://doi.org/10.1002/2016GL070023; https://doi.org/10.1016/j.hal.2013.03.002; https://doi.org/10.1016/j.hal.2013.01.006; https://doi.org/10.1016/j.hal.2023.102431; https://doi.org/10.1016/j.ecss.2018.09.030; https://doi.org/10.1016/j.hal.2017.01.007; https://doi.org/10.1016/j.hal.2008.10.002
Alexandrium spp	Harbor of Syracuse, Ionian Sea; East China Sea; New South Wales; Northeast Atlantic / Northern Europe; Mediterranean; U.S. East Coast	~37.0–38.0° N, ~15.0–15.5° E; 29.0°-31.0°N, 122.0°-123.0°E; ~28–36° S, ~153–150° E; ~55–70° N, ~5°W–20°E; ~40–45° N, ~0–10°E; ~41–45°	Northern; Southern	2019; 2004–2007; 2005–2013; Multiple years; 2000s – 2010s	https://doi.org/10.4081/ijfs.2021.9062; Wang YF et al. (2018); https://doi.org/10.1016/j.marpolbul.2013.04.009; https://doi.org/10.1016/j.hal.2022.102335; https://doi.org/10.1016/j.hal.2021.101989; https://doi.org/10.3390/d13080396; https://doi.org/10.1016/j.hal.2020.101843; https://northeasthab.whoi.edu/habs/alexandrium/

		N, ~66–71°W			
Dinophysis spp	NW Iberia; Gulf of Mexico; German Bight / North Sea; Santa Catarina coast; Mediterranean; NW Europe / Atlantic coast; Port Underwood / Marlborough Sounds; Reloncaví / Patagonian fjords; Northeast USA / New England; Northern Gulf of Mexico; Bay of Biscay; Southeastern Australia	40°38.6′ N, 42°21.5′ N; ~ 25–29° N, ~ 85–95° W; ~ 54–55° N, ~ 7–8° E; ~ 26–28° S, ~ 48–49° W; ~ 40–41° N, ~ 8–9° E; ~ 44–55° N, ~ -10° to +5° E/W; 41.0°–41.5°S, 173.8°–174.2°E; ~41°–43°S, ~72°–74°W; ~41°–46°N, ~66°–71°W; ~29°–31°N, ~85°–89°W; ~44°–46°N, ~0°–2°W; ~34°–38°S, ~150°–154°E	Northern; Southern	2004-2013; 2007–2014; 2003; 2005; 2000s–2010s; across decades; 2003–2014; 2008–2010; 2010s	https://doi.org/10.1016/j.hal.2015.12.002; https://doi.org/10.1093/plankt/fbu070; https://doi.org/10.3354/meps259093; https://doi.org/10.1017/S0025315414001702; https://doi.org/10.4081/ijfs.2016.6095; https://doi.org/10.3390/toxins11020074; https://doi.org/10.3390/toxins11010019; https://doi.org/10.1016/j.hal.2013.03.005; https://doi.org/10.1111/j.1529-8817.2009.00791.x; https://doi.org/10.3390/md11082964; https://doi.org/10.1016/j.hal.2022.102253
Gambierdiscus spp	Canary Islands; Eastern Australia; Coastal Japan; Central Red Sea; U.S. Virgin Islands; Indian Ocean; Global	~28–30° N, ~13–18° W; ~15–35° S; ~24–36° N, ~122–145° E; ~18–22° N, ~38–40°	Northern; Southern; Northern & Southern (global)	2016; 2006–2011; 2012–2013; 2018–2021; 2013; ~2019/2020	https://doi.org/10.3390/toxins11070423; https://doi.org/10.3390/md16010007; https://doi.org/10.1371/journal.pone.0060882; https://doi.org/10.1016/j.hal.2017.08.005; https://coastalscience.noaa.gov/news/asynchrony-of-gambierdiscus-cell-abundance-and-toxicity-in-the-us-virgin-islands-implications-for-monitoring-and-prediction

		E; ~18°–19° N, ~64°–65° W; ~23–26° N, ~48–56° E; ~35° N to 35° S			-of-ciguatera/; https://doi.org/10.1017/S1755267213000675; https://doi.org/10.3390/toxins14070485
Trichodesmim spp.	Southwestern Tropical Pacific; Atlantic Ocean meridional transect; Arabian Sea & Bay of Bengal; Eastern Gulf of Mexico; Great Barrier Reef lagoon	5◦ S–25◦ S, 150◦ E–170◦ W; ~5°S–15°N; ~5°–20°N, ~60°–95°E; (27°32′ 50″N, 82° 46′ 55″W), (26°25′44″ N, 82°30′58″ W); ~14°–24°S, 144°–154°E	Southern; Both (Northern & Southern); Northern	1997–2010; 2007–2008; 2000s–2017; 2012–2013; 1997–2012	https://doi.org/10.5194/bg-8-3631-2011; https://doi.org/10.5194/bg-7-3167-2010; https://doi.org/10.1016/j.marpolbul.2017.06.002; https://doi.org/10.1111/1574-6941.12088; https://doi.org/10.1007/s13280-020-01460-3
Nodularia spp	Baltic Sea; Gulf of Finland; Kattegat / Öresund; Gippsland Lakes	57–59°N, 18–20°E; 56–58°N, 11–13°E; 59–60°N, 24–26°E; 54–60°N; 37.8–38.6°S, 147.5–148.6°E	Northern; Southern	2014; 2010; 2005; 2016–2018; 2010–2013	Jörgen Öberg (2014); https://doi.org/10.1038/s41598-022-14880-w; https://doi.org/10.1016/j.hal.2019.05.005; https://doi.org/10.3390/md11010001; https://doi.org/10.1016/j.hal.2007.05.007; https://doi.org/10.3390/md16040116; https://doi.org/10.3354/meps09843

427

Table S5 The top 30 countries and their major and secondary causative species of blooms in HAEDAT

Rank	Country	Major causative species	Count	Secondary causative species	Count	Total
1	France	*Dinophysis*	332	*Pseudo-nitzschia*	135	1215
2	United States	*Alexandrium catenella*	171	*Alexandrium*	159	1183
3	Spain	*Dinophysis acuminata*	380	*Pseudo-nitzschia australis*	106	1133
4	Portugal	*Dinophysis acuminata*	281	*Gymnodinium catenatum*	132	1011
5	Philippines	*Pyrodinium bahamense*	955	*Alexandrium*	19	981
6	Norway	*Alexandrium*	208	*Dinophysis acuta*	133	698
7	Canada	*Heterosigma akashiwo*	52	*Alexandrium catenella*	42	384
8	Japan	*Karenia mikimotoi*	77	*Margalefidinium polykrikoides*	25	363
9	United Kingdom	*Dinophysis*	111	*Alexandrium*	87	351
10	Slovenia	*Pseudo-nitzschia calliantha*	42	*Dinophysis*	38	340
11	Mexico	*Gymnodinium catenatum*	60	*Pyrodinium bahamense*	24	300
12	Sweden	*Nodularia spumigena*	133	*Dinophysis*	44	298
13	China	*Prorocentrum dentatum*	37	*Skeletonema costatum*	34	251
14	Ireland	*Dinophysis acuminata*	33	*Dinophysis acuta*	32	149
15	Korea	*Margalefidinium polykrikoides*	56	*Mesodinium rubrum*	8	109
16	Denmark	*Dinophysis acuminata*	21	*Dinophysis acuta*	7	106
17	Uruguay	*Dinophysis acuminata*	24	*Gymnodinium catenatum*	13	99
18	Germany	*Nodularia spumigena*	15	*Phaeocystis globosa*	10	96
19	Turkey	*Heterosigma akashiwo*	10	*Skeletonema*	6	85
20	Iceland	*Pseudo-nitzschia*	20	*Dinophysis*	18	76
21	Poland	*Nodularia spumigena*	56	*Heterocapsa triquetra*	6	75
22	Chile	*Alexandrium catenella*	46	*Dinophysis acuta*	5	74
23	Netherlands	*Phaeocystis*	28	*Dinophysis acuminata*	11	67
24	Peru	*Dinophysis caudata*	10	*Akashiwo sanguinea*	6	65
25	South Africa	*Alexandrium catenella*	13	*Dinophysis acuminata*	6	64
26	Australia	*Gambierdiscus*	12	*Noctiluca scintillans*	9	59
27	Argentina	*Alexandrium catenella*	15	*Alexandrium tamarense*	11	58
28	Indonesia	*Noctiluca scintillans*	16	*Pyrodinium bahamense*	11	51
29	Greece	*Noctiluca scintillans*	9	*Dinophysis acuminata*	4	48
30	Russian Federation	*Heterosigma akashiwo*	6	*Noctiluca scintillans*	5	48

Table S6 Annual average of human footprint index and population count within 0.1 × 0.1 pixel in the Northern and Southern Hemispheres

Year	Human footprint index (unitless)		Population count (people)	
	Northern Hemisphere	Southern Hemisphere	Northern Hemisphere	Southern Hemisphere
2003	6	2	78	34
2004	6	2	85	39
2005	6	2	93	41
2006	6	2	97	41
2007	6	2	98	41
2008	6	2	100	43
2009	7	2	102	44
2010	6	2	102	44
2011	6	2	104	50
2012	7	2	107	51
2013	7	2	109	51
2014	7	2	114	51
2015	7	2	118	53
2016	7	2	121	54
2017	7	2	128	57
2018	7	2	133	61
2019	7	2	142	64
2020	7	2	160	81

Table S7 Moran' I index test results

Year	Moran' I		Z-score		P-value	
	BAA	CBD	BAA	CBD	BAA	CBD
2003	0.4596	0.3762	10.0240	8.3352	0.0000	0.0000
2004	0.4521	0.4041	9.8791	8.9570	0.0000	0.0000
2005	0.4973	0.4556	10.8698	10.0608	0.0000	0.0000
2006	0.4562	0.4534	9.9627	10.0483	0.0000	0.0000
2007	0.4918	0.4532	10.7610	9.9987	0.0000	0.0000
2008	0.4768	0.4980	10.4506	11.0553	0.0000	0.0000
2009	0.5104	0.5291	11.1435	11.7021	0.0000	0.0000
2010	0.5082	0.4760	11.1235	10.5097	0.0000	0.0000
2011	0.5124	0.4101	11.2194	9.0678	0.0000	0.0000
2012	0.5121	0.4489	11.2259	9.9359	0.0000	0.0000
2013	0.5240	0.4979	11.4646	10.9018	0.0000	0.0000
2014	0.5219	0.4374	11.4403	9.7043	0.0000	0.0000
2015	0.4944	0.4479	10.8187	9.8412	0.0000	0.0000
2016	0.5242	0.4707	11.5262	10.3535	0.0000	0.0000
2017	0.5175	0.4134	11.3722	9.1326	0.0000	0.0000
2018	0.5037	0.4666	10.9682	10.1877	0.0000	0.0000
2019	0.4933	0.4246	10.7570	9.3097	0.0000	0.0000
2020	0.4762	0.4661	10.4170	10.2247	0.0000	0.0000

Table S8 Multicollinearity test results of BAA influencing factors in open water

	Unstandardized coefficient		Standardized coefficient			Collinearity statistics	
	B	Standard error	Beta	t	Significance	Tolerance	VIF
(constant)	-0.0410	0.0500		-0.8160	0.4150		
DSST	-0.1950	0.0330	-0.1880	-5.9360	0.0000	0.2900	3.4520
NWS	0.2970	0.0250	0.2880	12.0630	0.0000	0.5130	1.9500
PH	0.0500	0.0190	0.0480	2.5510	0.0110	0.8250	1.2120
PREC	0.2390	0.0210	0.2310	11.4480	0.0000	0.7180	1.3940
SA	0.3060	0.1540	0.0540	1.9910	0.0470	0.3910	2.5570

Dependent variable: BAA

Table S9 Multicollinearity test results of BAA influencing factors in continental coastal waters

	Unstandardized coefficient		Standardized coefficient			Collinearity statistics	
	B	Standard error	Beta	t	Significance	Tolerance	VIF
(constant)	-0.3700	0.0790		-4.6730	0.0000		
DSST	-0.2890	0.0700	-0.2690	-4.1420	0.0000	0.1100	9.0940
NWS	0.3560	0.0370	0.3450	9.7060	0.0000	0.3670	2.7270
pH	-0.1550	0.0280	-0.1510	-5.4450	0.0000	0.6050	1.6530
Prec	0.0850	0.0270	0.0820	3.1910	0.0010	0.6990	1.4300
SR	0.0760	0.0560	0.0700	1.3530	0.1760	0.1710	5.8500
Sa	1.2220	0.1710	0.2590	7.1500	0.0000	0.3530	2.8300
Pop	0.0940	0.0360	0.0830	2.5900	0.0100	0.4550	2.1990
HFP	-0.0350	0.0310	-0.0330	-1.1190	0.2630	0.5400	1.8520
Urban	0.0140	0.0310	0.0130	0.4710	0.6380	0.6190	1.6160
Shurb	-0.0590	0.0290	-0.0550	-2.0370	0.0420	0.6400	1.5610
Grass	-0.1350	0.0320	-0.1080	-4.2160	0.0000	0.7000	1.4280
Forest	-0.0790	0.0300	-0.0700	-2.6460	0.0080	0.6710	1.4900
Crop	0.0560	0.0320	0.0480	1.7550	0.0790	0.6140	1.6280

Dependent variable: BAA

Table S10 Multicollinearity test results of CBD influencing factors in open water

	Unstandardized coefficient		Standardized coefficient			Collinearity statistics	
	B	Standard error	Beta	t	Significance	Tolerance	VIF
(constant)	-0.3120	0.0510		-6.1540	0.0000		
pH	-0.0400	0.0210	-0.0390	-1.9350	0.0530	0.7870	1.2710
Prec	0.2800	0.0240	0.2700	11.718	0.0000	0.5890	1.6990
Sa	1.2930	0.1610	0.2290	8.0490	0.0000	0.3860	2.5920
SR	-0.5270	0.0350	-0.5130	-14.972	0.0000	0.2650	3.7700
DWS	0.1380	0.0210	0.1330	6.7240	0.0000	0.7950	1.2590
Dependent variable: CBD							

Table S11 Multicollinearity test results of BAA influencing factors in continental coastal waters

	Unstandardized coefficient		sStandardized coefficient			Collinearity statistics	
	B	Standard error	Beta	t	Significance	Tolerance	VIF
(constant)	-0.4010	0.0850		-4.6950	0.0000		
DSST	-0.5450	0.0750	-0.4800	-7.2720	0.0000	0.1110	9.0280
pH	-0.1570	0.0310	-0.1450	-5.1230	0.0000	0.6040	1.6540
Prec	-0.0940	0.0290	-0.0850	-3.2480	0.0010	0.6970	1.4350
SR	0.2590	0.0610	0.2260	4.2670	0.0000	0.1710	5.8400
Sa	1.1890	0.1850	0.2380	6.4400	0.0000	0.3520	2.8400
Pop	0.1010	0.0390	0.0840	2.5850	0.0100	0.4540	2.2040
HFP	0.0380	0.0340	0.0340	1.1220	0.2620	0.5400	1.8530
Urban	-0.0240	0.0330	-0.0200	-0.7170	0.4740	0.6200	1.6130
Shurb	-0.0050	0.0310	-0.0040	-0.1630	0.8710	0.6490	1.5400
Grass	-0.0270	0.0340	-0.0200	-0.7760	0.4380	0.7040	1.4210
Forest	-0.0650	0.0320	-0.0540	-2.0220	0.0430	0.6700	1.4920
Crop	0.0610	0.0340	0.0500	1.7770	0.0760	0.6170	1.6200
DWS	0.3340	0.0400	0.3010	8.3750	0.0000	0.3720	2.6860

Dependent variable: CBD

Table S12 Related parameters of GTWR model results

	BAA		CBD	
	Coastal water	Open water	Coastal water	Open water
Bandwidth	49.2254	56.2623	49.2254	56.2623
Residual squares	124.8067	415.3834	117.4729	603.2072
Sigma	0.2801	0.3876	0.2717	0.4671
AICc	467.4107	2607.4145	371.0622	3638.9218
R^2	0.7769	0.7520	0.8032	0.6770
Adjusted R^2	0.7750	0.7516	0.8015	0.6764
Spatio-temporal distance ratio	3.0342	3.0342	3.0342	3.0342

Table S13 Non-remote sensing parameters for monitoring marine blooms

Location	Definition of phytoplankton blooms	Sampling frequency	Chl a concentration	Cell density	Reference
Five estuaries in Denmark	Blooms were defined as chlorophyll a observations deviating significantly from a normal seasonal cycle; the frequency and magnitude of these deviating observations.	biweekly	3.2 to 82.6 ug/L	No definition	Carstensen J et al., 2007
Southern Ocean	No definition.	No definition	>300 mg/m^2	No definition	Schine C M S et al., 2021
The Central Yellow Sea, China	Phytoplankton blooms are important ecological processes, which can be expressed either as high biomass or high primary production.	daily	greater than 2 μg/L	No definition	Sun J et al.,2013
Thau Lagoon, a typical productive coastal site on the edge of the Mediterranean Sea	A bloom was identified as a period 1) that started with at least 2 consecutive days of positive growth rates and 2) where the sum of net growth rates over at least 5 consecutive days was positive. The end of the bloom was the day before 5 consecutive days with negative growth.	weekly	No definition	No definition	Trombetta T et al., 2019
Chesapeake Bay	Phytoplankton blooms are hereafter defined as the time when the cell abundance of a single taxon exceeded $0.5*10^6$ cells/L for a period of 3 d or longer and/or daily chl a concentrations exceeded 44 μg/L, twice the average chl a concentration for the nearby Chesapeake Bay monitoring program station LFB01 from 2000 to 2009.	daily	No definition	$>10^6$ cells/L	Morse R E et al.,2014
The open southern Adriatic Sea	No definition	15 research cruises	1.65 – 1.85 mg/m^3	$1.6*10^5$cells/L	Jasprica N et al.,2022
The West Florida Shelf (WFS) of the eastern Gulf of Mexico	No definition	daily	~0.5 μg/L	$>10^5$ cells/L	Hu C et al., 2022

REFERENCES:

1. Gobler, C. J., Doherty, O. M. and Hattenrath-Lehmann, T. K. et al. (2017). Ocean warming since 1982 has expanded the niche of toxic algal blooms in the North Atlantic and North Pacific oceans. Proc. Natl. Acad. Sci. USA. 114(19): 4975-4980. https://doi.org/10.1073/pnas.1619575114.
2. Hunter-Cevera, K. R., Neubert, M. G., and Olson, R. J., et al. (2016). Physiological and ecological drivers of early spring blooms of a coastal phytoplankter. Science. 354(6310): 326-329. https://doi.org/10.1126/science.aaf8536.
3. Beaugrand, G. and Kirby, R. R. (2018). How do marine pelagic species respond to climate change? Theories and observations. Annu Rev Mar Sci. 10(1): 169-197. https://doi.org/10.1146/annurev-marine-121916-063304.
4. Doney, S. C., Fabry, V. J., and Feely, R. A. et al. (2009). Ocean acidification: the other CO2 problem. Annu Rev Mar Sci. 1(1): 169-192. https://doi.org/10.1146/annurev.marine.010908.163834.
5. Allen, J. T., Brown, L., and Sanders, R. et al. (2005). Diatom carbon export enhanced by silicate upwelling in the northeast Atlantic. Nature. 437(7059): 728-732. https://doi.org/10.1038/nature03948.
6. Kuttippurath, J., Sunanda, N., and Martin, M.V. et al. (2021). Tropical storms trigger phytoplankton blooms in the deserts of north Indian Ocean. npj Clim Atmos Sci. 4(1): 11. https://doi.org/10.1038/s41612-021-00166-x.
7. Tang, W., Llort, J., and Weis, J. et al. (2021). Widespread phytoplankton blooms triggered by 2019–2020 Australian wildfires. Nature. 597:370–375 . https://doi.org/10.1038/s41586-021-03805-8.
8. Shi, X., Zou, Y., and Zhang, Y. et al. (2024). Salinity decline promotes growth and harmful blooms of a toxic alga by diverting carbon flow. Global Change Biology. 30(6): e17348. https://doi.org/10.1111/gcb.17348.
9. Luijendijk, E., Gleeson, T. and Moosdorf, N. (2020). Fresh groundwater discharge insignificant for the world's oceans but important for coastal ecosystems. Nat Commun. 11(1):1260. https://doi.org/10.1038/s41467-020-15064-8.
10. Pade, N., Michalik, D., and Ruth, W. et al. (2016). Trimethylated homoserine functions as the major compatible solute in the globally significant oceanic cyanobacterium Trichodesmium. Proc. Natl. Acad. Sci. USA. 113(46): 13191-13196. https://doi.org/10.1073/pnas.1611666113.
11. Ajani, P. A., Savela, H., and Kahlke, T. et al. (2023). Response of planktonic microbial assemblages to disturbance in an urban sub-tropical estuary. Water Res. 243: 120371. https://doi.org/10.1016/j.watres.2023.120371.
12. Wells, M. L., Trainer, V. L., and Smayda, T. J. et al. (2015). Harmful algal blooms and climate change: Learning from the past and present to forecast the future. Harmful algae. 49: 68-93. https://doi.org/10.1016/j.hal.2015.07.009.
13. O'brien, R. M. (2007). A caution regarding rules of thumb for variance inflation factors. Quality & quantity, 41(5), 673-690. https://doi.org/10.1007/s11135-006-9018-6.
14. Wang, J., Li, X., and Christakos, G. et al. (2010). Geographical Detectors-Based Health Risk Assessment and its Application in the Neural Tube Defects Study of the Heshun Region, China. International Journal of Geographical Information Science, 24(1), 107–127. https://doi.org/10.1080/13658810802443457
15. Granger C. W. J. (1969). Investigating causal relations by econometric models and cross-spectral

methods. Econometrica: journal of the Econometric Society.: 424-438. https://doi.org/10.2307/1912791.